Electronic Supplementary Material of

High-Throughput Underwater Elemental Analysis μJ-Laser-Induced Breakdown Spectroscopy at kHz Repetition Rate: Part II, Understanding High Repetition-Rate from a Fundamental Perspective

Boyang Xue[1, 2], Yi You[2†], and Jens Riedel[2]

[1] Ocean University of China, Qingdao, Shandong 266100, China
[2] Federal Institute for Materials Research and Testing (BAM), Berlin D-12489, Germany

[†]Corresponding Author: Yi You, Email: yi.you@bam.de, Tel: +49-30-81405542

1. Fundamental characterization of the laser-induced cavitation bubble

Comparing to the acquisition rate of the iCCD camera, which is ~1 frame/s, the rep.-rate of the laser is much faster. To avoid overlap of two images, *i.e.* two cavitation bubbles appear in the same image, the prescaler on the digital delay generator was configured to send camera-trigger signal every two seconds. For instance, the prescaler was set to 20'000 at 10 kHz laser rep.-rate. Based on this timing control, every image only contains once single lasing event. To avoid pulse-to-pulse variation, the 10 images were recorded for each delay time for averaged-bubble size. One example image is shown in Figure S1a.

After recording the image, the first image at the delay time of 1μs, at which the plasma emission was no longer observable, was used as background. At this delay time, the cavitation bubble did not yet appear. After background subtraction, the punch mark and other optical interferences became no longer significant comparing to the bubble (*cf.* Figure S1b).

The following step was to extract the row of pixels near the bubble center (*cf.* Figure S1c). The feature of the bubble can be readily identified. In specific, the bubble area appears to be very close to instrument background. Thus, we arbitrarily selected an intensity threshold, -1×10^4 counts, to generate the final binary image (*cf.* Figure S1d). After carefully selecting the area of interests, *i.e.* masking out other features that could clutter the bubble feature, the total area in terms of pixels can be determined. We then calculated the equivalent bubble diameter based on this area.

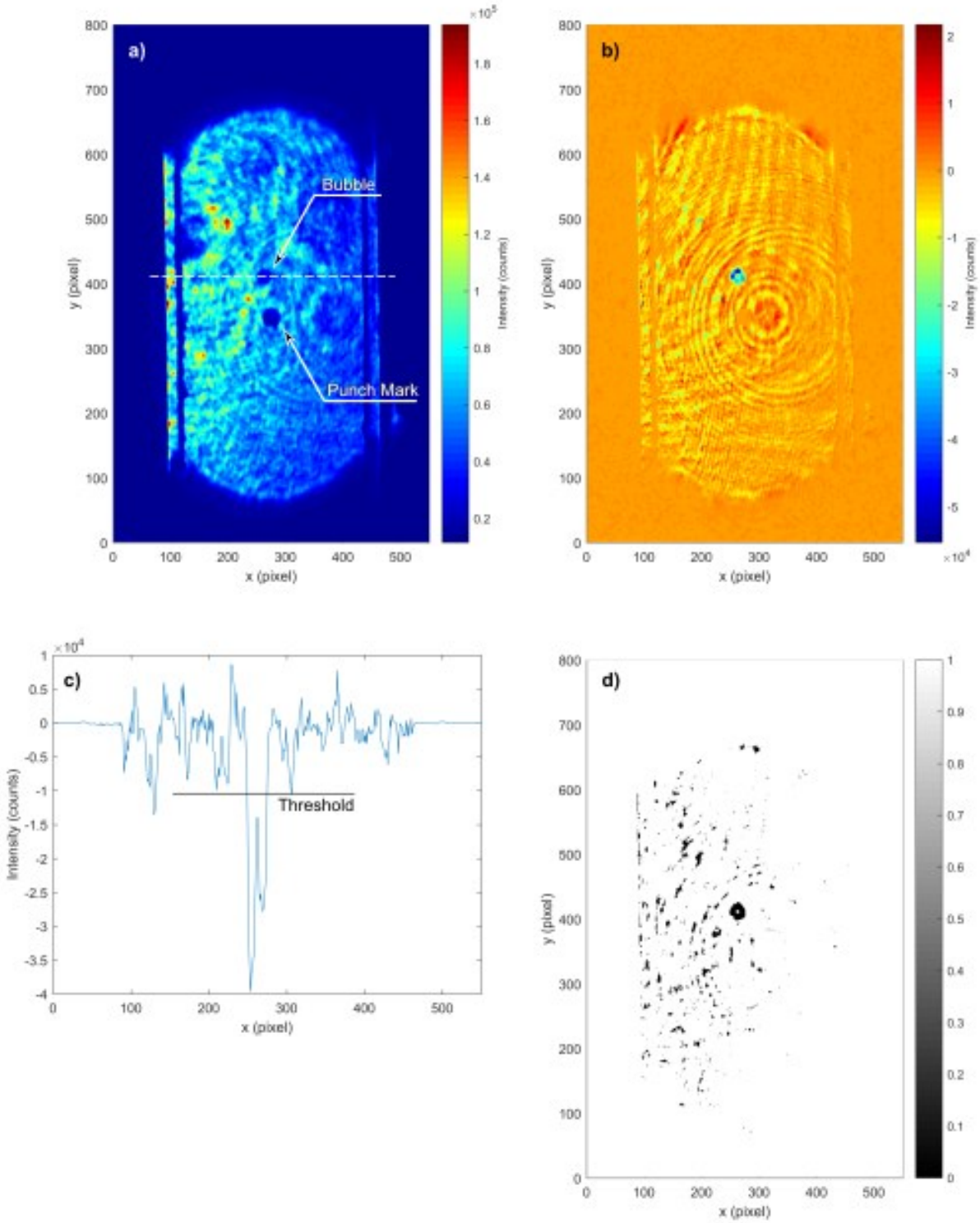

Figure S 1. Shadowgraphic images of laser-induced cavitation bubble at the delay time of 15 µs of 10 Hz rep.-rate. a) original image, b) image after background subtraction, c) line value at y-pixel number of 413, denoted by the white dashed line in a), and d) binary image for bubble size determination.

2. Lifetime of laser-induced cavitation bubbles at various pulse energies

Comparing to the shadowgraphic approach with an iCCD camera, it is more efficient and simpler to use a photomultiplier to probe the lifetime of cavitation bubbles at various conditions. Note that the temporal size evolution cannot be accurately determined by a photomultiplier.

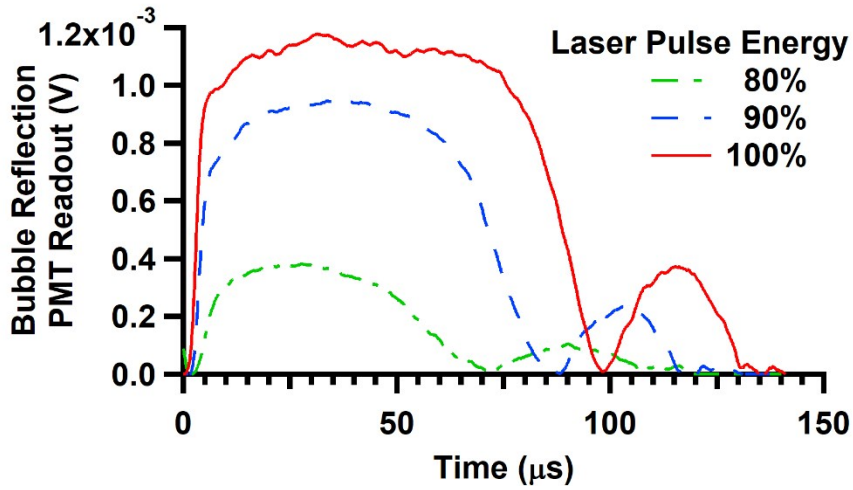

Figure S 2. Life cycles of laser-induced cavitation bubble at different laser pulse-energy at 1 kHz rep.-rate.

3. Rep.-rate response of H-α as a function of per-pulse laser energy

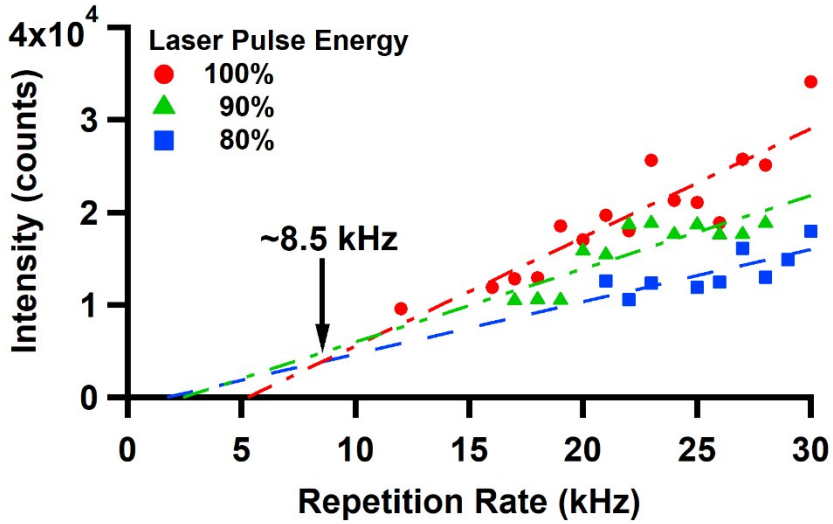

Figure S 3. Pulse-averaged H-α signals as functions of rep.-rate and laser pulse energy.

4. Plasma ignition probability as a function of rep.-rate

To acquire the information regarding the ignition probability, an automatic platform was built in-house to gain higher data density, better reproducibility and improved statistical validity. Instead of capturing the spectrally resolved signal (*i.e.* from a spectrometer), a plasma ignition can be determined through its broadband emission, which is comparably stronger and easier to detect.

Thus, a PMT was used to capture such signals. Note that the PMT used here is only sensitive up-to 680 nm (E717-63, Hamamatsu); the 1064 nm fundamental radiation should not interfere with the ignition determination. The analog signal was sent through a BNC cable to an USB-oscilloscope (HT6022B, Hantek Co. Ltd., Qingdao, China) with a termination of 1 kΩ. Commonly, the PMT should be terminated with 50 Ω to reflect the true transient signal. However, we were only interested whether there was a plasma being ignited. The use of 1 kΩ termination significantly prolonged the signal on the oscilloscope to compensate the low sample rate of the oscilloscope (10 MSa/S). Specifically, to resolve a 200 ns duration transient plasma signal, the sample rate on an analog-to-digital converter (ADC) should be at least 400 MSa/s, which is not possible on this device. The advantage of using such a low-resolution oscilloscope is to exploit its application programming interface (API), where the data can be recorded on a computer (denoted as CPU in Figure S4) and analyzed in real-time. The workflow used here can be described as: the controlling computer generates a random sequence of rep.-rates; at each rep.-rate, the laser operate at this condition for 5 s to allow the oscilloscope to capture the signal during this interval; the computer analyzes the signal and save the results corresponding to the operating condition (*i.e.* rep.-rates and pulse energy). Notably, the plasma ignition probability can be quite sensitive to the change of experimental condition, such as temperature. Thus, the rep.-rate sweep at such a high rate was performed in a random fashion. In this case, the cumulative effect, such as liquid temperature increment due to insufficient thermal dissipation, is only reflected as random fluctuations in the final results.

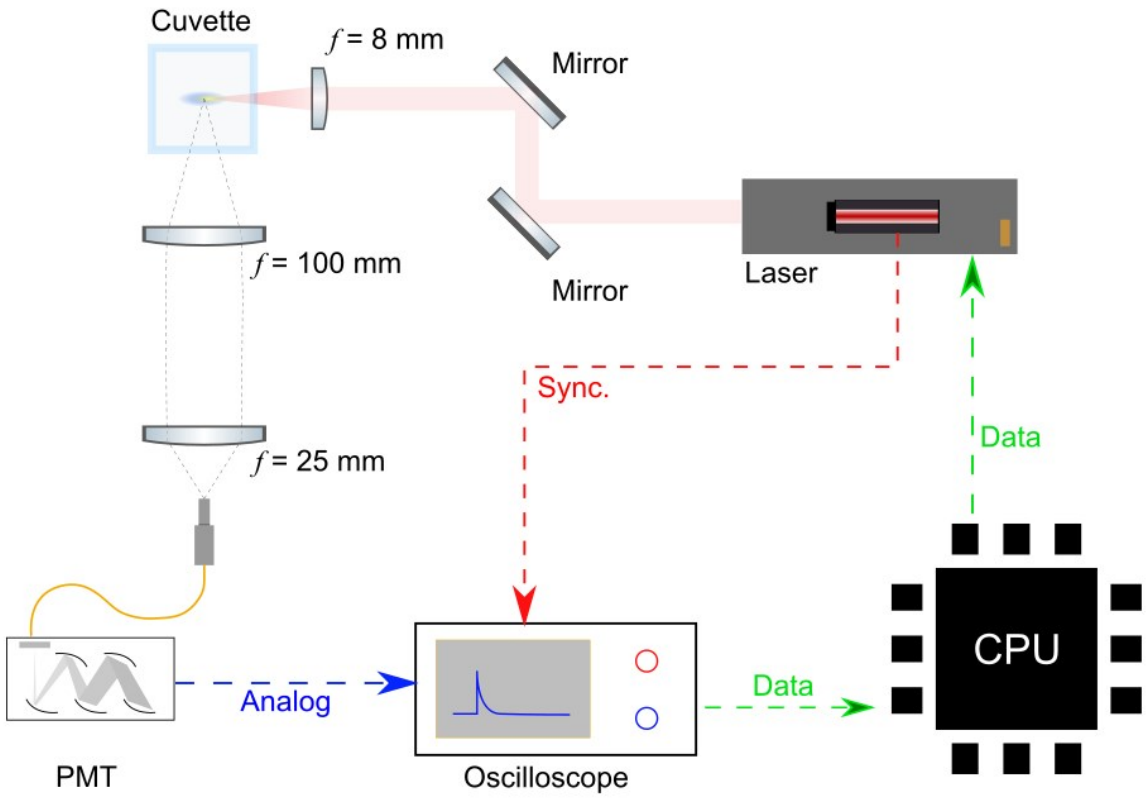

Figure S 4. Schematic of automated rep.-rate sweep platform.

The oscilloscope records the synchronization output (master clock) and the PMT output. From these sets of data, the ignition probability can be calculated by dividing the number of PMT pulses by the number of lasing pulses. Importantly, the ignition probability determined by a PMT is significantly (~20%) higher than that from an iCCD probably due to the high sensitivity of a PMT.

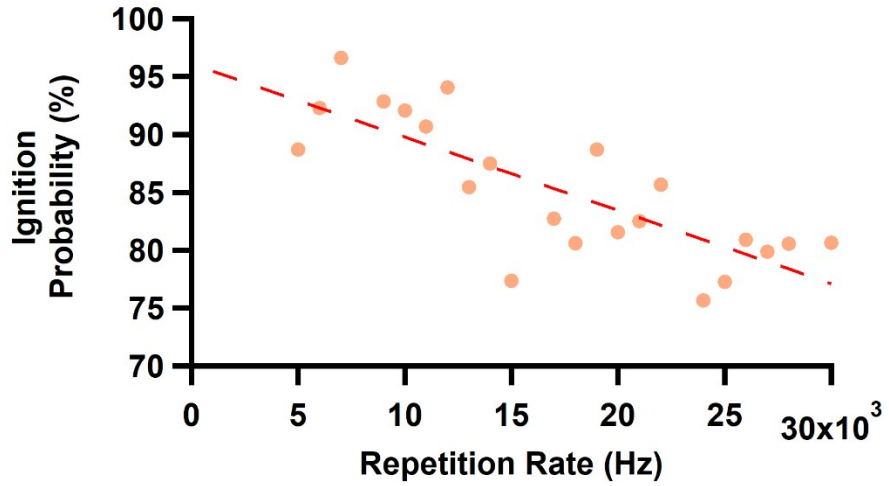

Figure S 5. Ignition probability as a function of rep.-rate at 100% pulse energy (600 μJ/pulse).

5. Vector projection analysis for spectral categorization

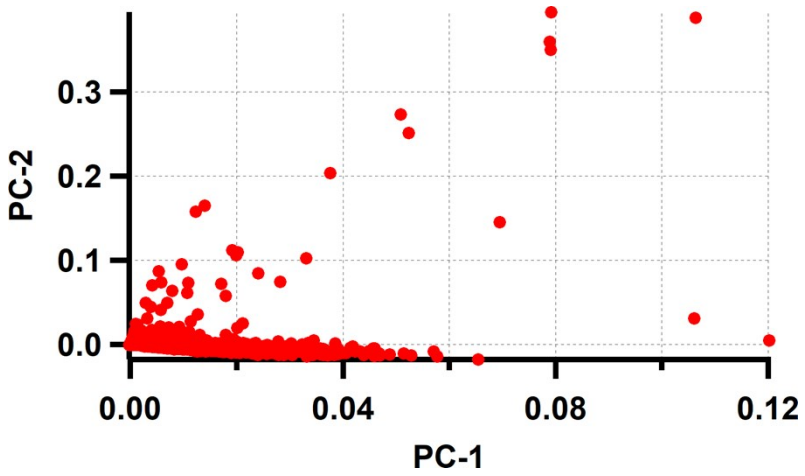

Figure S 6.PCA analysis of the 10’000 spectra at 20 kHz.

Comparing to the vector projection method described in the main text, the conventional PCA can somehow separate the spectra into different categories as well. However, the vector projection is directly related to the emission intensities of characteristic emissions that can be associated to physical processes involved in plasma lifespan. Thus, the categorization of vector appeared to be more linearly distributed in the PC domain comparing to the regular PCA. Additionally, the loadings corresponding to PC-1 and PC-2 (*cf.* Figure S7 and S8, respectively), mixed the features in the two categories of spectra. For instance, the Loading-1 contains the emission region that

covers H-α at 656 nm, which is also covered by Loading-2. In this scenario, the vector projection avoided this interference. As such, we choose to use vector projection.

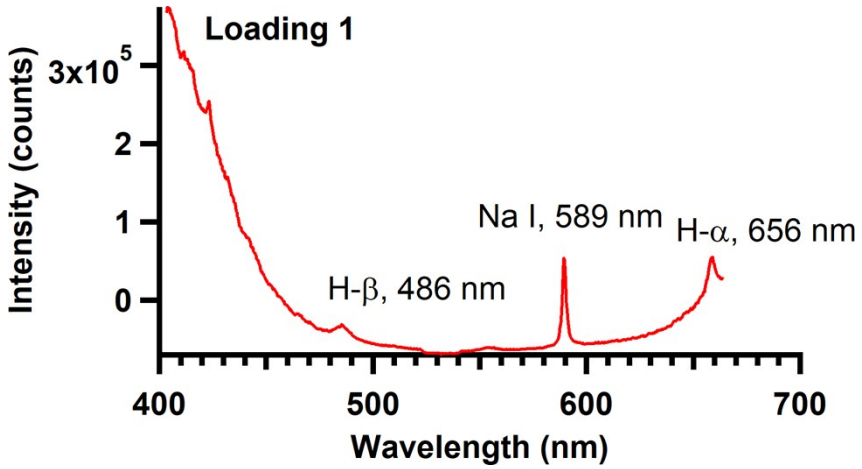

Figure S 7. Loading 1 corresponding to PC-1.

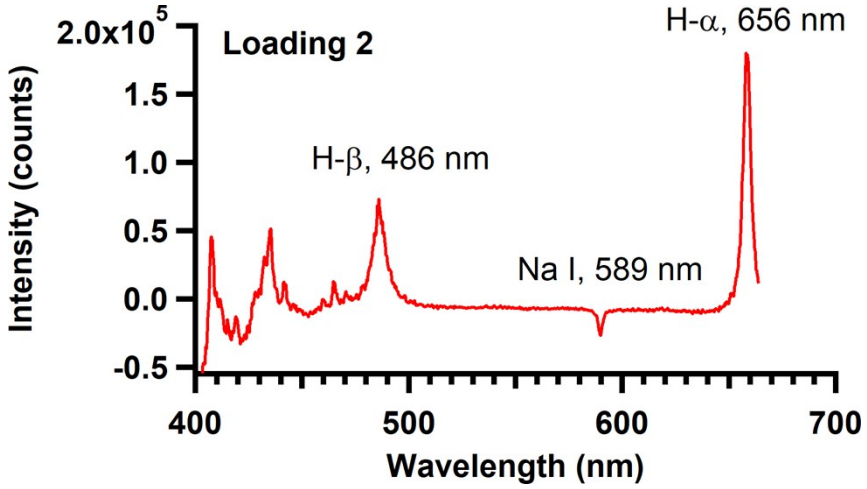

Figure S 8. Loading 2 corresponding to PC-2.

6. Delayed activation of iCCD MCP

To demonstrate the MCP decay and relative timing, we used 20 kHz as a model rep.-rate (*cf.* Figure S9). The laser profile was measured with a photodiode (DET-201, Thorlabs) through probing the residual laser after passing the cuvette (*cf.* Figure S9, red trace). The plasma emission was detected with the PMT (*cf.* Figure S9, blue trace). The transient signal was recorded with an oscilloscope (DL9102, Yokogawa) at 2.5 GSa/s (*i.e.* 0.4 ns temporal resolution). The camera trigger was denoted with the black arrow (*cf.* Figure S9, black arrow). The experimental geometry was the same as described in main text Figure 1a.

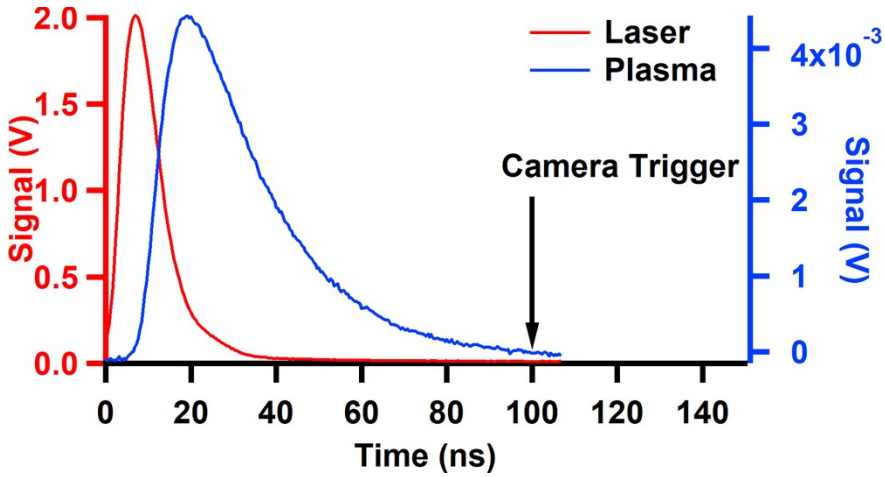

Figure S 9. Relative trigger timing for spectral acquisition.

At this experimental condition, the same setup was used. Instead, the optical fiber that was connected to the MCP was connected to the spectrometer (Sharmrock SR168, Andor). Instead of full vertical binning (FVB) mode, which is commonly used for spectral acquisition, image mode was used to reveal the MCP activation delay. As demonstrated here (*cf*. Figure S10), the white circle in the figure was used to mark activated (outside the circle) and un-activated (inside the circle) areas. To access this effect, the gate width was changed from 10 ns to 100 ns. When the gate width was set to 10 ns, only the outer perimeter was activated (*cf*. Figure S10, 10 ns). Based on the grating alignment (we were unable to tune this factor), the spectral information was allocated on the first ~400 pixels vertically. With only 10 ns gate width, the spectral information between 200-800 horizontal pixels was completely absent. Similar effect can be seen for 20 and 30 ns gate width. By estimating the radius decrement of the un-activated area, a minimal gate width of 56 ns is required to activate the entire MCP. As such, the minimal gate width used in this study was 60 ns.

As a very unfortunate consequence, we shifted the gate time forward (towards the early broadband emission) in order to capture the spectral information that was occupied in the x-center part of the iCCD. As a result, the early activated outer perimeter was exposed to broad band emission. Experimentally, spectra similar to Figure 6c was captured. In normal operation, where multiple lasing events were averaged (in either time- or pulse- averaged modes), the gate time can be set to a later time avoiding the broadband emission. However, in order to capture very weak individual plasma emission, this compensation had to be made. Any late gate time would have resulted in empty spectra that contained no information at all.

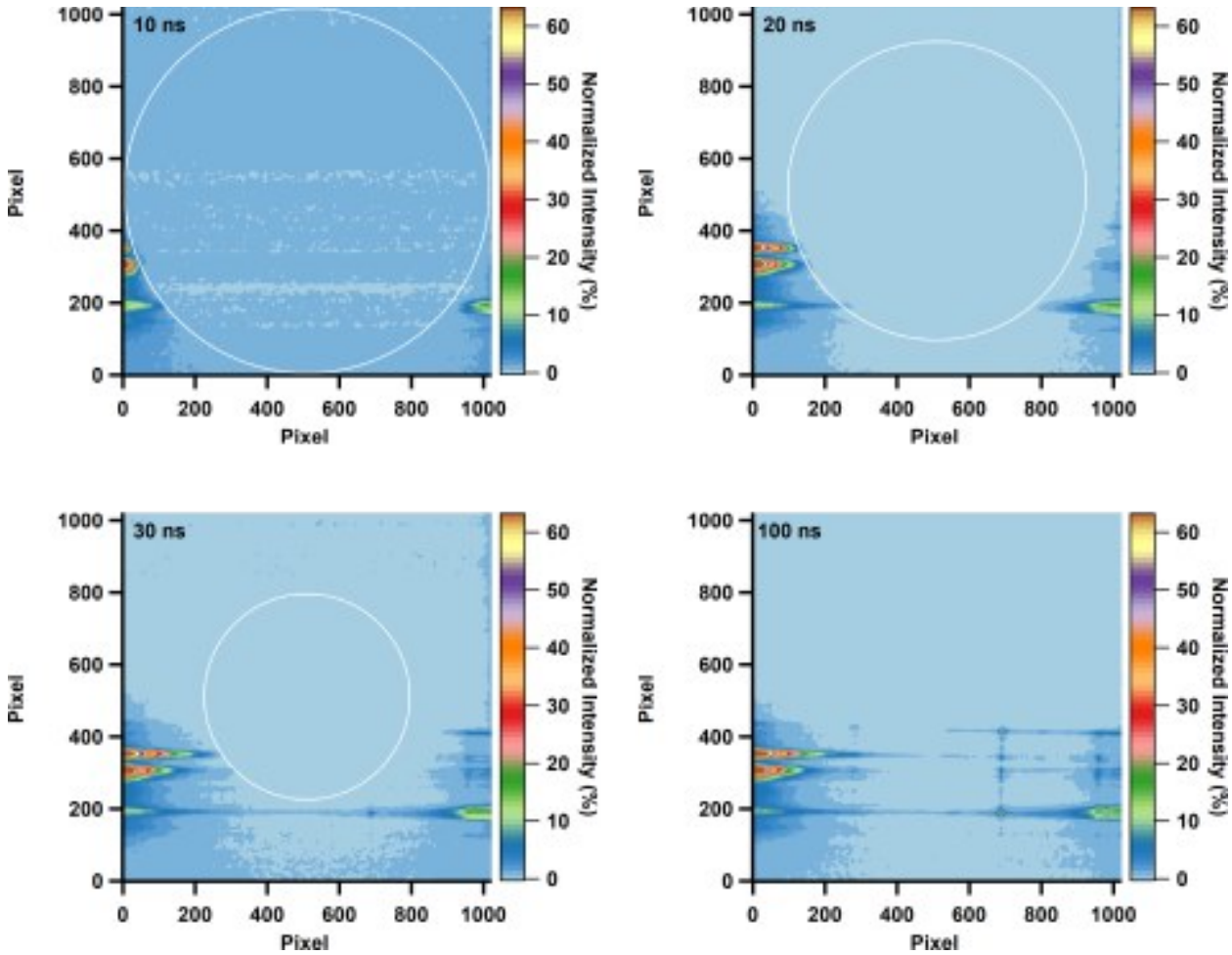

Figure S 10. Demonstration of MCP activation delay.

7. Vector projection analysis of individual spectra and type-II spectral partition

In addition to the 20 kHz example rep.-rate, additional rep.-rates at 2, 8, 13.5, 15, 20 kHz were investigated. To demonstrate the presence of type-II spectra, water was used as the sample solution without addition of other ions (*e.g.*, Na^+ and Ca^{2+}). Each vector projection maps (*cf.* Figure S11) contains data points corresponds to 2000 lasing event. Notably, the total duration of acquiring 2000 spectra at 1 spectra/s acquisition rate resulted in a total experiment time of ~35 minutes. For such a small cuvette, the high laser flux would have increased the liquid temperature significantly if the experiment runs continuously. Thus, the cuvette was air cooled by blowing high volumetric flow compressed air for temperature control. To minimize the thermal accumulation, 100 spectra were recorded at a time. Thereafter, the cuvette was allowed to cool in air for 10 min. Importantly, the PC-2 was calculated based on the area of H-α. Comparing to the peak value of H-α intensity (*cf.* Figure 6b), this number is significantly higher.

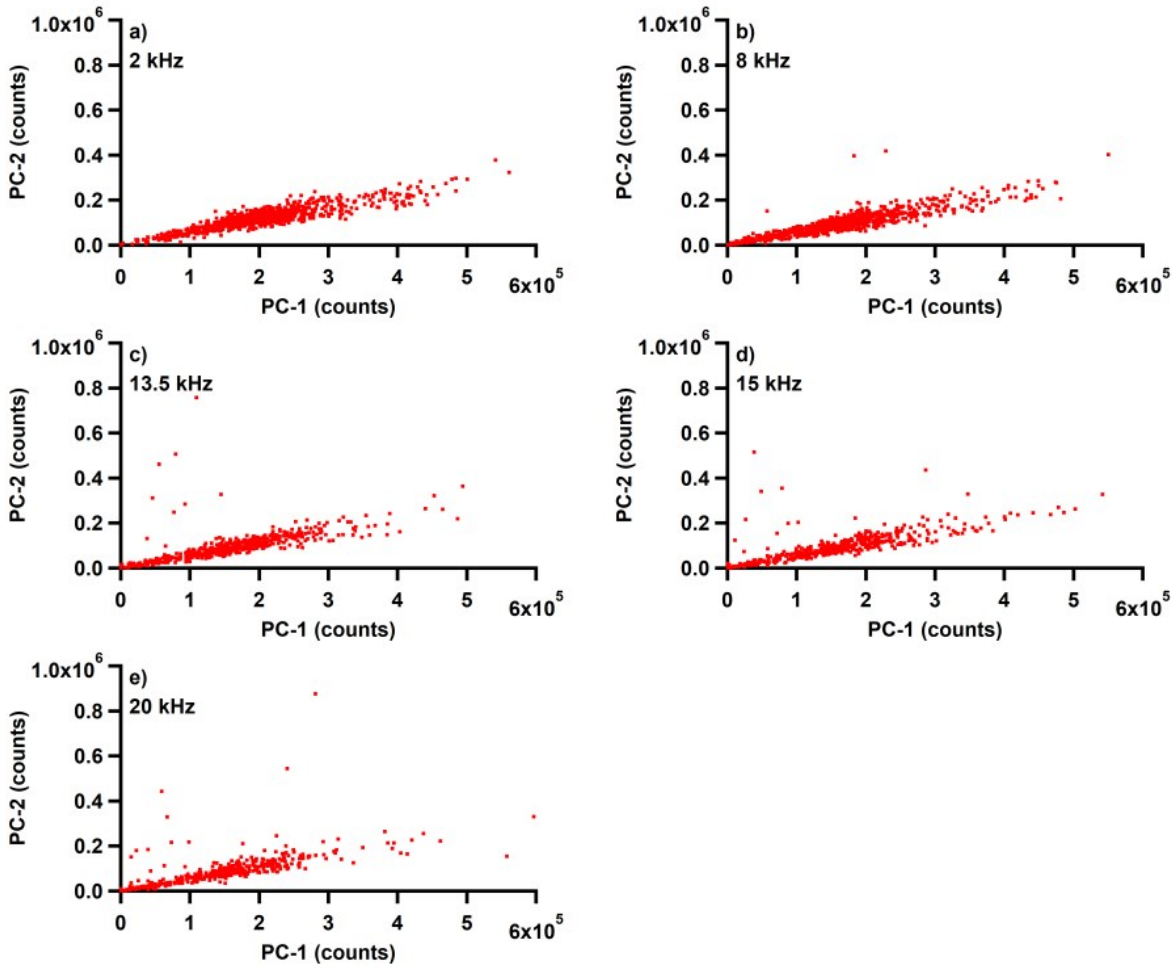

Figure S 11. Vector projection maps for various rep.-rates. Subplot a) to e) represent the maps for their corresponding rep.-rates.

The pool of 10'000 spectra can hardly accurate the type-II partition. The ones shown in Figure S11 possess even less numbers of event involved. However, it can be accessed through intensity-based calculation. The example emission spectrum at 20 kHz is shown in Figure S12.

The typical emission intensity of Na I from a single lasing event is roughly 4.5×10^4 counts. Similarly, the intensity of H I at 656 nm is 3.9×10^4 counts. A ratio can be then calculated with:

$$P = \frac{3.1\times10^4 / 3.9\times10^4}{3.1\times10^4 / 3.9\times10^4 + 3.6\times10^5 / 4.5\times10^4} \times 100\% = 0.97\% \qquad \text{Eq. S1}$$

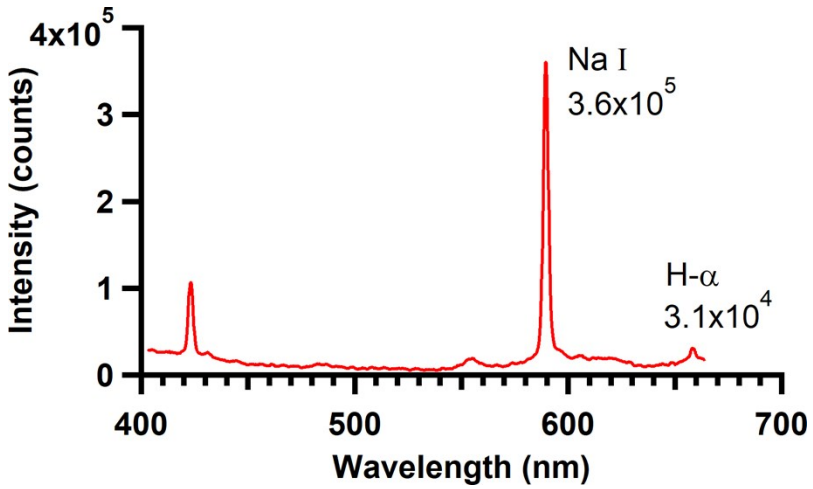

Figure S 12. Example emission spectrum of 20 kHz with 400 ppm Na^+ and Ca^{2+} each.

From each vector projection map, the variation on the PC-2 axis (*i.e.* area of 656 nm) varied in very similar ranges for different rep.-rates (*cf.* Figure S11cde). Due to the low probability of type-II excitation pathway, we used 20 kHz as an example rep.-rate, which involved 10'000 lasing events (*cf.* Figure S13a).

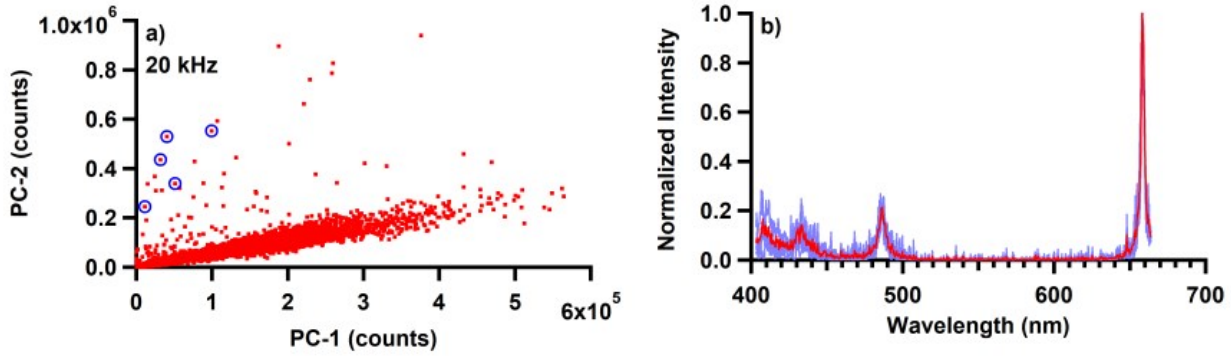

Figure S 13. Extracted type-II spectra at 20 kHz rep.-rate. a) pseudo-PCA plot and b) extracted type-II spectra. The solid trace in b) represent all the data points marked with blue circle in a); the red solid trace is the average of the five spectra.

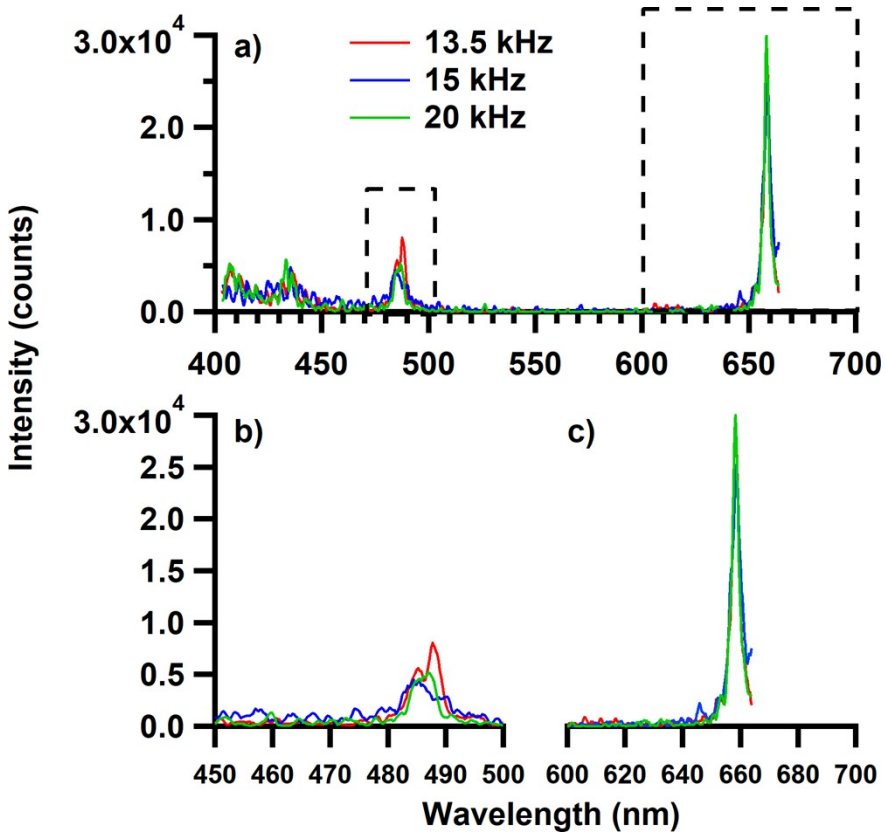

Figure S 14. Direct comparison between the type-II spectra at example rep.-rates. a) shows the averaged type-II spectra of the rep.-rates according to the figure legend. b) and c) are the zoomed areas for visual comparison.

8. H-α as a function of inter-pulse interval

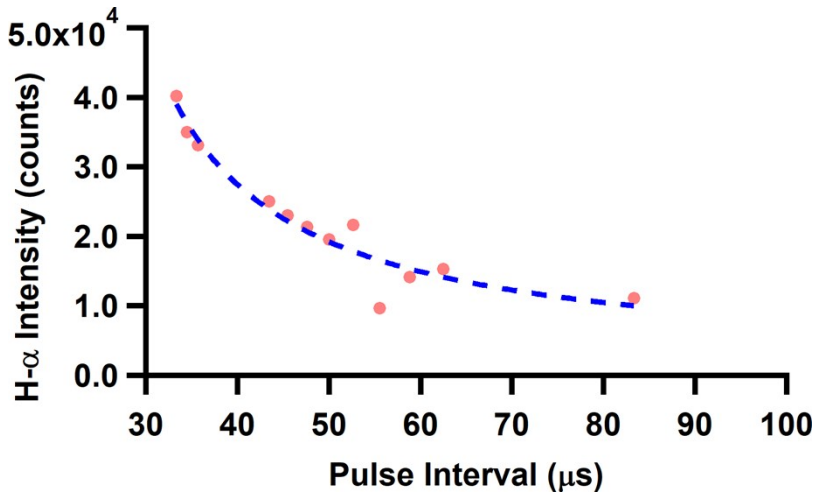

Figure S 15. H-α as a function of interval between two consecutive laser pulses.

9. External perturbation

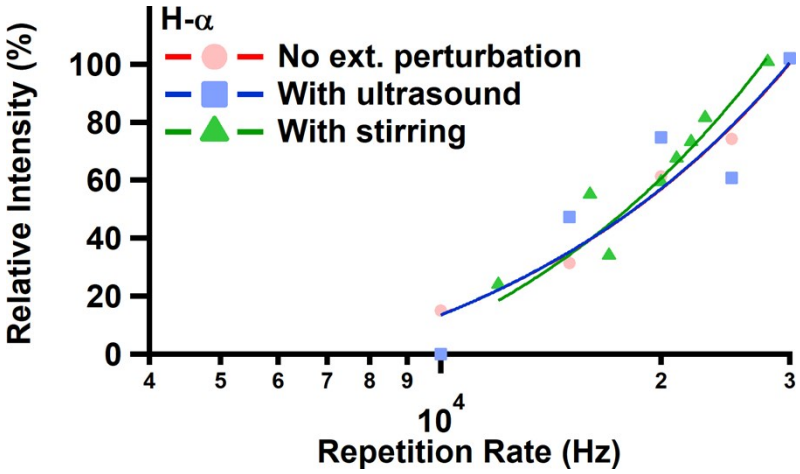

Figure S 16. Intensity response as a function of rep.-rate under different conditions. The red, blue, and green markers/traces represent H-α signal response without external perturbation, with near-field ultrasound, and with stirring, respectively. All the data points were fitted with linear functions, which were translated into curves on logarithmic scale. The blue and solid red traces overlapped in this figure.

To determine the general trend of emission lines corresponding dissolved species (*cf.* Figure 7), curve fittings were applied with the model shown below:

$$f(x) = a_1 \cdot \left(1 - e^{-k_1(x - x_1)}\right) + a_2 \cdot e^{-k_2 \cdot (x - x_2)} \qquad \text{Eq. S2}$$

where $f(x)$ is the fitted model, the independent variable x here is the rep.-rate, the a_1 and a_2 are the coefficients for the two pathways shown in this equation, the pumping pathway is: $\left(1 - e^{-k_1(x - x_1)}\right)$, in which k_1 and x_1 are the rate coefficient and x-offset, respectively; the draining pathway is given by: $e^{-k_2 \cdot (x - x_2)}$, where k_2 and x_2 are the rate coefficient and x-offset for this channel.